Experimental evidence for melt partitioning between olivine and orthopyroxene in partially molten harzburgite

Kevin J. Miller[1,2], Wen-lu Zhu[1], Laurent G. J. Montési[1], Glenn A. Gaetani[3], Véronique Le Roux[2], and Xianghui Xiao[4]

[1]Department of Geology, University of Maryland at College Park, College Park, Maryland, USA, [2]Now at Department of Geophysics, Stanford University, Stanford, California, USA, [3]Department of Geology and Geophysics, Woods Hole Oceanographic Institution, Woods Hole, Massachusetts, USA, [4]Advanced Photon Source, Argonne National Laboratory, Lemont, Illinois, USA

Abstract Observations of dunite channels in ophiolites and uranium series disequilibria in mid-ocean ridge basalt suggest that melt transport in the upper mantle beneath mid-ocean ridges is strongly channelized. We present experimental evidence that spatial variations in mineralogy can also focus melt on the grain scale. This lithologic melt partitioning, which results from differences in the interfacial energies associated with olivine-melt and orthopyroxene-melt boundaries, may complement other melt focusing mechanisms in the upper mantle such as mechanical shear and pyroxene dissolution. We document here lithologic melt partitioning in olivine-/orthopyroxene-basaltic melt samples containing nominal olivine to orthopyroxene ratio of 3 to 2 and melt fractions of 0.02 to 0.20. Experimental samples were imaged using synchrotron-based X-ray microcomputed tomography at a resolution of 700 nm per voxel. By analyzing the local melt fraction distributions associated with olivine and orthopyroxene grains in each sample, we found that the melt partitioning coefficient, i.e., the ratio of melt fraction around olivine to that around orthopyroxene grains, varies between 1.1 and 1.6. The permeability and electrical conductivity of our digital samples were estimated using numerical models and compared to those of samples containing only olivine and basaltic melt. Our results suggest that lithologic melt partitioning and preferential localization of melt around olivine grains might play a role in melt focusing, potentially enhancing average melt ascent velocities.

1. Introduction

Field observations in ophiolites [e.g., *Kelemen et al.*, 1995] and geochemical data [e.g., *Condomines et al.*, 1981; *Newman et al.*, 1983; *Volpe and Hammond*, 1991; *Iwamori*, 1994] collected from mid-ocean ridge basalt and abyssal peridotites suggest that the transport of melt toward the ridge axis likely takes place in high melt fraction, high-permeability conduits [*Kelemen et al.*, 1997; *Jull et al.*, 2002]. Two mechanisms have previously been proposed to organize melt on length scales comparable to the compaction length of partially molten rock: the reaction infiltration instability (RII) [e.g., *Daines and Kohlstedt*, 1994; *Kelemen et al.*, 1995; *Aharonov et al.*, 1995; *Spiegelman et al.*, 2001; *Pec et al.*, 2015] and deformation-induced melt segregation [e.g., *Holtzman et al.*, 2003; *Holtzman and Kohlstedt*, 2007; *Allwright and Katz*, 2014; *Qi et al.*, 2015]. The former is a consequence of the positive feedback between melt flux and pyroxene dissolution, and the later results from the anisotropic viscosity of rock undergoing shear deformation. In this study, we present experimental evidence that interfacial energy gradients resulting from spatial variation in mineralogy can also concentrate and organize melt at the grain scale. Here we show that this process, called lithologic melt partitioning [*Watson*, 1999], can operate in harzburgitic rocks under pressure and temperature conditions similar to the Earth's upper mantle.

At grain scale, the minimization of surface energy determines the equilibrium melt geometry. For a pack of uniform, isotropic grains containing a single mineral phase, melt forms a uniform network of prismatic melt tubules [*Smith*, 1948, 1964; *Bulau et al.*, 1979; *Waff and Bulau*, 1979; *von Bargen and Waff*, 1986]. However, most of the Earth's upper mantle is polymineralic, composed primarily of olivine and pyroxene—orthopyroxene (opx) and clinopyroxene (cpx)—as well as minor mineral phases, all of which have different wetting properties [e.g., *Toramaru and Fujii*, 1986]. Therefore, the equilibrium melt distribution for a polymineralic aggregate is not straightforward to predict.
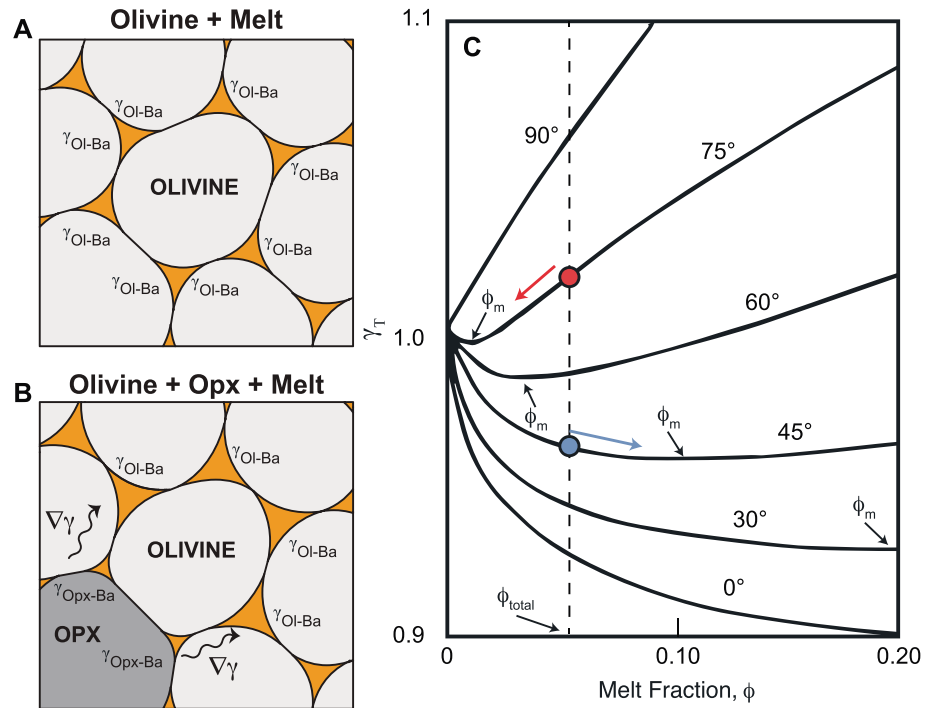
Figure 1. Schematic diagram illustrating the minimum-energy melt fractions for olivine and opx in a close system containing a finite amount of melt. Modified from *Park and Yoon* [1985] and *Watson* [1999]. (a) Schematic diagram of an aggregate containing only olivine and basaltic melt. Local melt fraction is the same for every grain. (b) Schematic diagram of an aggregate containing olivine, opx, and basaltic melt. Spatial variations in the surface energy distribution, resulting from different mineral component, cause the basaltic melt to partition unevenly between olivine (higher melt fraction) and opx (lower melt fraction). (c) Total surface energy contained in a melt-bearing rock system normalized by the total surface energy contained in a melt-free system plotted as a function of melt fraction for various dihedral angles. The dotted line represents the total melt fraction contained in an example system. In a homogeneously mixed olivine-opx-basaltic melt aggregate, local melt fractions associated with olivine (blue circle) and opx (red circle) will adjust to minimize the energy of the system. Arrows with ϕ_m indicate the minimum-energy melt fraction for an open system that is exposed to an infinite melt reservoir.

Park and Yoon [1985] calculated the total surface energy of a grain pack as a function of melt fraction and dihedral angle. Dihedral angle θ is the standard metric for mineral wettability [e.g., *Cooper and Kohlstedt*, 1982] and is defined by

$$cos\left(\frac{\theta}{2}\right) = \frac{\gamma_{ss}}{2\gamma_{sm}} \tag{1}$$

where γ_{ss} and γ_{sm} are the surface energy densities of the solid-solid and solid-melt interface.

The total interfacial energy is given by

$$E = \frac{1}{2}\gamma_{ss}A_{ss} + \gamma_{sm}A_{sm} \tag{2}$$

where A_{ss} and A_{sm} are the areas of the solid-solid and solid-melt interface. *Park and Yoon* [1985] considers dodecahedral grains with a uniform grain size l_0 and a regular, space-filling melt network. In the absence of melt, the interfacial energy for each grain is

$$E_0 = 4\sqrt{2}\ l_0^2\gamma_{ss} \tag{3}$$

Melt can decrease or increase the total interfacial energy, as shown in Figure 1. It is clear from Figure 1 that for a given dihedral angle, effectively a given mineralogy, there is a unique melt fraction that minimizes the total energy of the grain pack. If the system is displaced from the minimum-energy melt fraction and open to a melt reservoir, it follows from Figure 1 that the system will balance its melt content so as to minimize the total interfacial energy. In particular, an open system that is undersaturated with respect to the minimum-energy

melt fraction ($\phi < \phi_{min}$) will draw melt from the reservoir, whereas an oversaturated system ($\phi > \phi_{min}$) will expel melt. Systems with lower dihedral angles tend to favor a higher melt fraction.

As the interfacial energy is different for each mineral, melt distribution in a polymineralic aggregate is expected to become progressively heterogeneous. Consider several monomineralic aggregates, each with initially the same melt fraction (e.g., $\phi = \phi_{total}$ in Figure 1c), but with different mineral types, and therefore mineral aggregates. When the aggregates are put in contact, melt can redistribute between the aggregates. The slope of the energy versus melt fraction curves of Figure 1c imply that the energy of the system as a whole decreases if the melt content of the aggregate with highest dihedral angle decreases and that of the aggregate with lowest dihedral angle increases. Using an expression for the total interfacial energy of two aggregates in contact under the constraint that the total melt content is fixed, it is possible to determine that for the lowest energy condition, the mineral aggregate with lowest dihedral angle have at least twice the melt fraction of the mineral aggregate with highest dihedral angle [*Park and Yoon*, 1985; *Cheadle*, 1989; *Lupulescu and Watson*, 1999].

This behavior, known as lithologic melt partitioning, was experimentally confirmed in fluorite/quartz + H_2O and clinopyroxene/quartz + H_2O systems, where fluid partitioned in a 5 to 2 ratio and 3 to 1 ratio, respectively. However, similar partitioning was not observed in experiments using olivine, opx, and melt [*Watson*, 1999]. Though the distance separating the olivine- and opx-rich regions was similar (a few millimeters) to the fluorite-quartz experiments, basaltic melt is 4 orders of magnitude more viscous than water, suggesting that melt partitioning would be not be measurable given an experiment duration of less than 6 days. Here we document lithologic partitioning in an olivine-opx-melt system where the mineral phases are intimately mixed, as in the upper mantle.

If olivine and opx grains are in close proximity, the distance over which melt must be transported to exhibit lithologic melt partitioning is reduced. However, it is not possible to use the theoretical interface energy estimate of a single mineral/melt aggregate from *Park and Yoon* [1985] as no region is constituted of a single mineral type. Therefore, the intensity of lithologic partition should be less than estimated from the end-member mineralogies. Nevertheless, given the marked difference between dihedral angle of olivine-olivine-melt and opx-opx-melt junctions ($\theta_{ol-ol-m} \sim 41°$ [*Cooper and Kohlstedt*, 1984] and $\theta_{opx-opx-m} \sim 70°$ [*Toramaru and Fujii*, 1986]), we should be able to observe a grain-scale melt distribution that spatially correlates with mineralogy.

In this study, we measured the lithologic melt partitioning in harzburgitic rocks using a novel approach. Experimental charges, composed of various proportions of olivine, opx, and basaltic melt, were synthesized in solid-media piston-cylinder apparatuses. Olivine and opx grains were homogeneously mixed, so that lithologic melt partitioning took place at a scale of few grains (i.e., tens of microns), much less than the millimeter scale of partitioning in the experiments of *Watson* [1999]. Cores were drilled from the experimental charges and imaged using synchrotron-based X-ray microcomputed tomography (μCT). The high-resolution, three-dimensional (3-D) images constituted virtual rock samples on which grain size distribution, local melt fraction distribution, and transport properties, both permeability and electrical conductivity, were numerically quantified.

2. Methods

2.1. Sample Preparation of Harzburgite Samples

Harzburgite samples were prepared by hot isostatic pressing of a mixture containing oxides and natural, high-alumina basalt. The solid proportion mixture was prepared by homogenizing oxides mixed in proportion such that olivine (forsterite) and opx (enstatite) crystals would have the same chemistry as those found in a natural harzburgite collected from the Southwest Indian Ridge [*Dick*, 1989]. For each melt fraction, the oxide proportions were adjusted to maintain a nominal 3 to 2 olivine to opx volume ratio, although measured volume fractions from subvolumes varied significantly. The chemicals and their proportions used in making the oxide mixtures are reported in Table 1.

Not all of the elements needed in harzburgite synthesis could be added to the mix as oxides. For example, calcium was added in carbonate form ($CaCO_3$). The mix was homogenized for six cycles, 1 h each, using an automatic agate mortar and pestle. Upon completion, we applied a decarbonation procedure to convert the carbonates to oxides. To decarbonate the mixture, we placed it in a furnace at an initial temperature of

Table 1. Starting Weights and Drying Conditions of Oxide and Carbonate Used to Synthesize Harzburgite With a 3 to 2 Olivine to Opx Ratio

Component	Drying Conditions	Measured Weight (g)
SiO_2	28 h at 1000°C	5.03010
TiO_2	No drying	0.00090
Al_2O_3	28 h at 1000°C	0.13627
Fe_2O_3	1 h at 800°C	0.91690
MnO_2	2 h at 800°C	0.01649
MgO	216 h at 1000°C	4.65014
$CaCO_3$	4 h at 400°C	0.16765
Na_2CO_3	No drying	0.00074
K_2CO_3	No drying	0.00077
NiO	2 h at 800°C	0.01961

300°C. The furnace temperature was raised to 850°C at 100°C/h and held at 850°C for a minimum of 24 h. After the mixture was decarbonated, pulverized natural basalt was added in various proportions to produce total volume melt fractions of 0.02, 0.05, 0.10, and 0.20 when melted. The same homogenization procedure was repeated for every oxide-basalt mixture.

For each melt fraction, ~36 mg of the oxide-basalt mixture was cold-pressed into a cylindrical pellet using a 0.91 t press and placed into a graphite capsule (Figure 2a). Capsules were dried overnight at 400°C to remove surface H_2O from the experimental charges so that the charges were nominally anhydrous. Charges were placed in solid-medium piston-cylinder apparatuses and brought up to 1.5 GPa and 1350°C using the cold piston-in technique [*Johannes et al.*, 1971]. Details about the uncertainty in pressure and temperature can be found in *Zhu et al.* [2011].

Upon completion of the piston-cylinder runs, the experimental charges were quenched by turning off the heating source while maintaining a steady flow of cold water through the space surrounding the pressure vessel. Water was not in contact with the sample at any time.

The field of view of the X-ray μCT device was ~1 mm, so we drilled 1 mm cylindrical cores from each experimental charge along the cylindrical axis (Figure 2b). The top of the sample was denoted by a polished surface that we used for scanning electron microscope and electron diffraction spectroscopy to ensure that the correct minerals formed.

2.2. Imaging Procedure

The workflow of image acquisition, preprocessing, and data reduction procedures is illustrated in Figure 3. Our objective was to map the 3-D distribution of olivine, opx, and melt in each experimental charge.

The very small density contrasts at olivine-opx, olivine-basalt, and opx-basalt boundaries warranted a novel imaging procedure, which involved a combination of absorption-contrast [e.g., *Johns et al.*, 1993] and phase-contrast [*Chapman et al.*, 1997] imaging techniques. Cylindrical harzburgite samples were imaged using a synchrotron light source at beamline station 2BM-A at the Advanced Photon Source, Argonne National Laboratory. A monochrometer was used to select a narrow energy spectrum centered at 24.4 keV. The sample
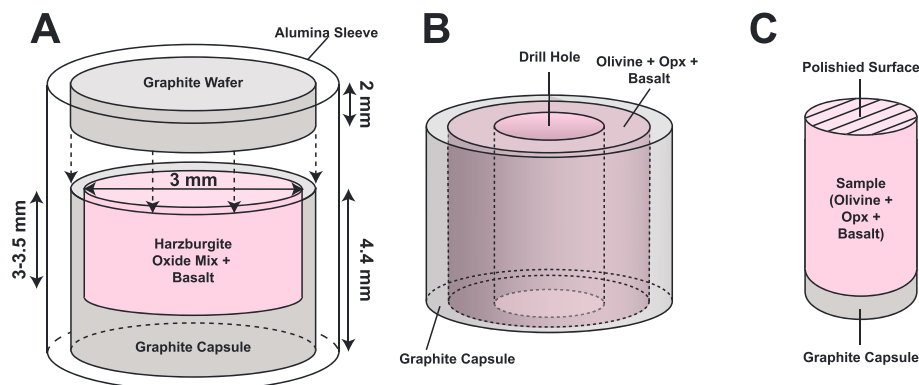
Figure 2. Schematic diagram of experimental setup before and after sintering. (a) Starting materials before sintering. The graphite capsule (gray), which is packed with the powdered olivine/basalt mixture (pink), is placed in an alumina sleeve with a graphite wafer as a lid. (b) Sample assembly after sintering. One side of the sample assembly is cut and the surface of the sintered aggregate is polished. (c) The hole in the sample assembly illustrates where the sample is taken for X-ray imaging. Hash marks represent the polished surface.
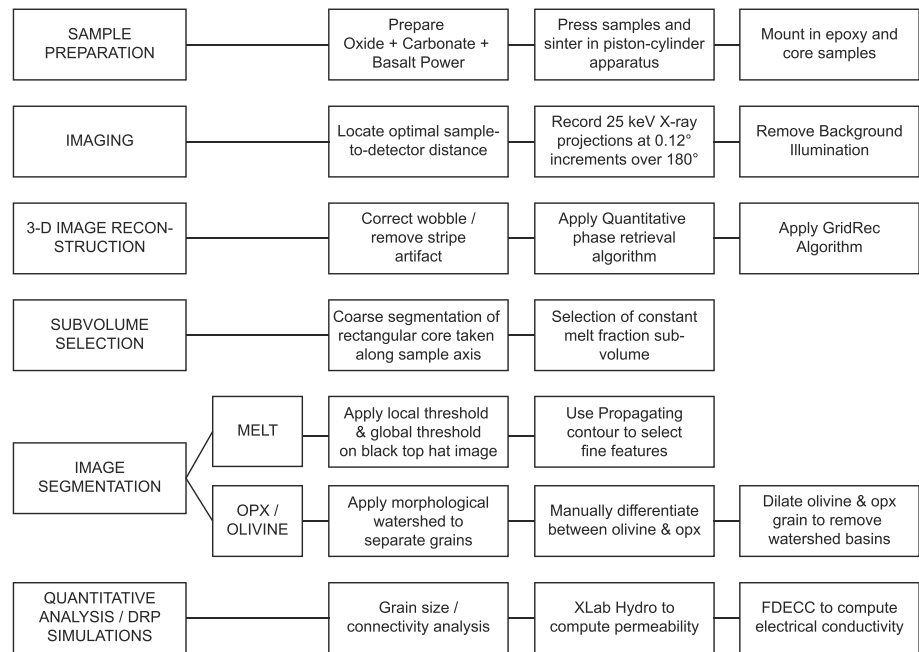
Figure 3. Workflow for reducing tomography data, quantifying morphology, and computing material properties.

was rotated 180° through the X-ray beam, and at every 0.12° increment, X-ray projections were recorded using a CCD camera. The sample-to-detector distance was 60 mm for every scan. Each projection contained information about the X-ray absorption and phase shift integrated along the trajectory of the X-ray. Prior to reconstruction, the background illumination was removed from each projection.

TomoPy [*Gürsoy et al.*, 2014], an open-sourced, Python-based software, was used to reconstruct the 3-D data sets from the 2-D projections. First, a stripe-removal algorithm based on *Münch et al.* [2009] was applied. A quantitative phase retrieval algorithm [*Paganin et al.*, 2002] was used to simultaneously recover the X-ray absorption and diffraction signal. Finally, GridRec [*Dowd et al.*, 1999] was used to perform the tomographic reconstruction. In the resulting gray scale image, olivine (lightest granular phase), opx (darkest granular phase), and quenched basaltic melt (dark interstitial phase) were clearly distinguishable. We show a tomographic slice taken perpendicular to the cylindrical axis of the sample in Figure 4.

2.3. Image Segmentation

Following *Miller et al.* [2014, 2015] and *Watson and Roberts* [2011], smaller subsets of data, which we call subvolumes, were cropped from each reconstructed 3-D image. Each subvolume was chosen in relatively homogeneous regions without large decompression fractures or artificially enhanced edges. Fractures were unintentionally generated during unloading but were not present under in situ run conditions. Grain edges were highlighted by the diffraction-based edge enhancing techniques [*Fitzgerald*, 2000].

In order to characterize the melt distribution, each gray scale subvolume was converted to an 8 bit label image; i.e., gray scale voxels were assigned integer values 1, 2, or 3 for basaltic glass, olivine, or opx, respectively. We developed a semiautomated workflow to segment the data using the 3-D analysis software Avizo®. First, a trial segmentation of the melt was performed using a combination of Avizo®'s local thresholding module and top-hat global threshold. Thin decompression fractures were manually removed from the image by overlapping the trial segmentation with an image mask. The image mask was computed by a sequential morphological erosion and dilation of the melt geometry using a $2 \times 2 \times 2$ voxel^3 ball-shaped kernel.

Subtle contrasts at the olivine-opx interfaces, bright imaging artifacts at the grain edges, and long-wavelength variations in the background gray scale prevented us from applying the same local threshold technique used for segmentation of melt to differentiate opx and olivine grains. Instead, we used a morphological watershed transformation to separate grains and then handpicked opx grains from the aggregate based on their gray scale value. Grains that were imperfectly separated using this technique were adjusted
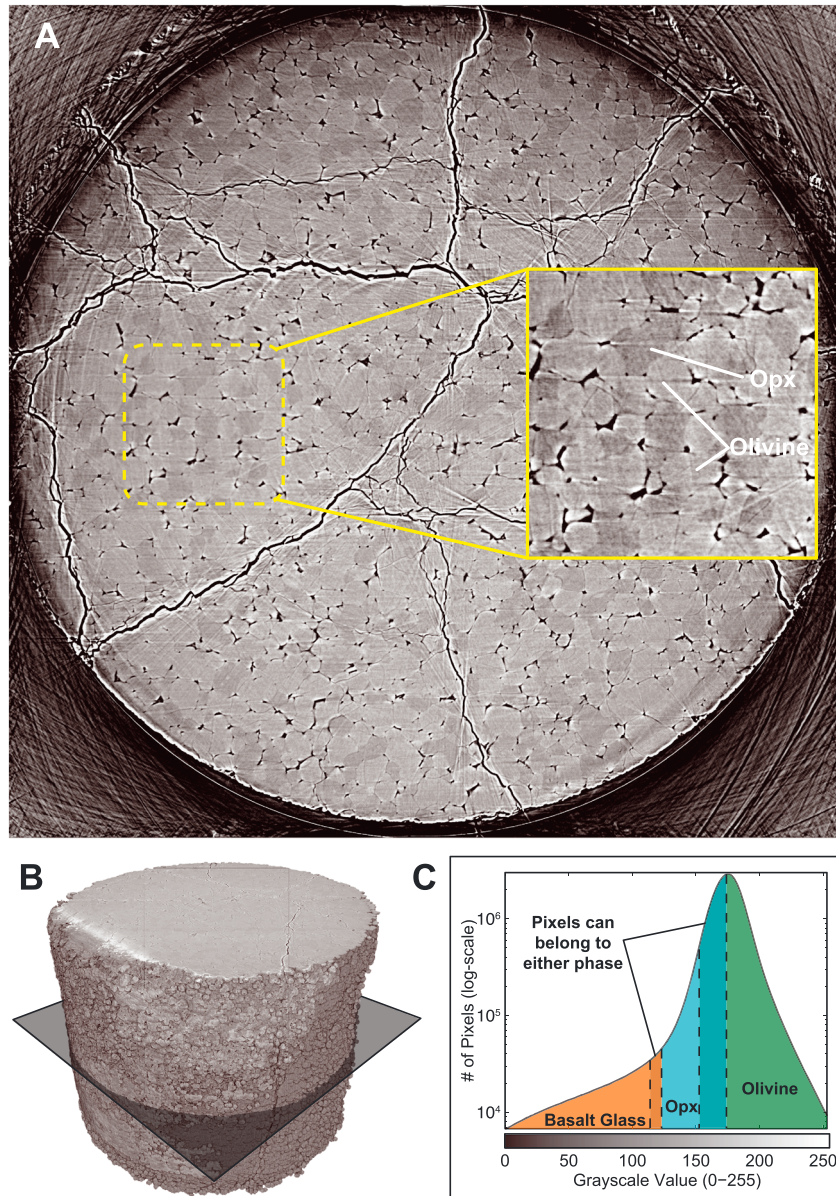
Figure 4. Visualization of the X-ray μCT data. (a) Tomography slice from a harzburgite sample with ~5 vol % quenched basaltic melt (glass). On the right is a close-up of the tomography slice. Olivine (light granular phase), opx (dark granular phase), and basaltic glass (dark interstitial phase) are clearly visible. (b) View of whole sample. The dark plane represents the location of the displayed tomography slice. (c) Histogram of gray scale values in a subvolume cropped from the sample.

using Avizo®'s propagating contour tool. Once all of the opx grains were differentiated from olivine, the watershed basins were removed by a simultaneous dilation of the olivine and opx images. To remove jagged edges, which are artifacts of the morphological watershed tool, the resulting 8 bit image was smoothed using a $3 \times 3 \times 3$ voxel^3 Gaussian kernel. Three-dimensional volume renderings of the label images are given in Figure 5. The result of the grain separation and image segmentation is compared to an original gray scale image in Figure 6. The resulting image is an accurate segmentation of the melt, olivine, and opx.

## 2.4. Quantification of Local Melt Fraction Distribution

Though a homogeneous mixture of olivine and opx reduced the amount of time required to reach a steady state microstructure, it complicated the evaluation of the characteristic melt fraction associated with each mineral phase, since adjacent olivine and opx grains shared the interstitial melt. Therefore, we created a
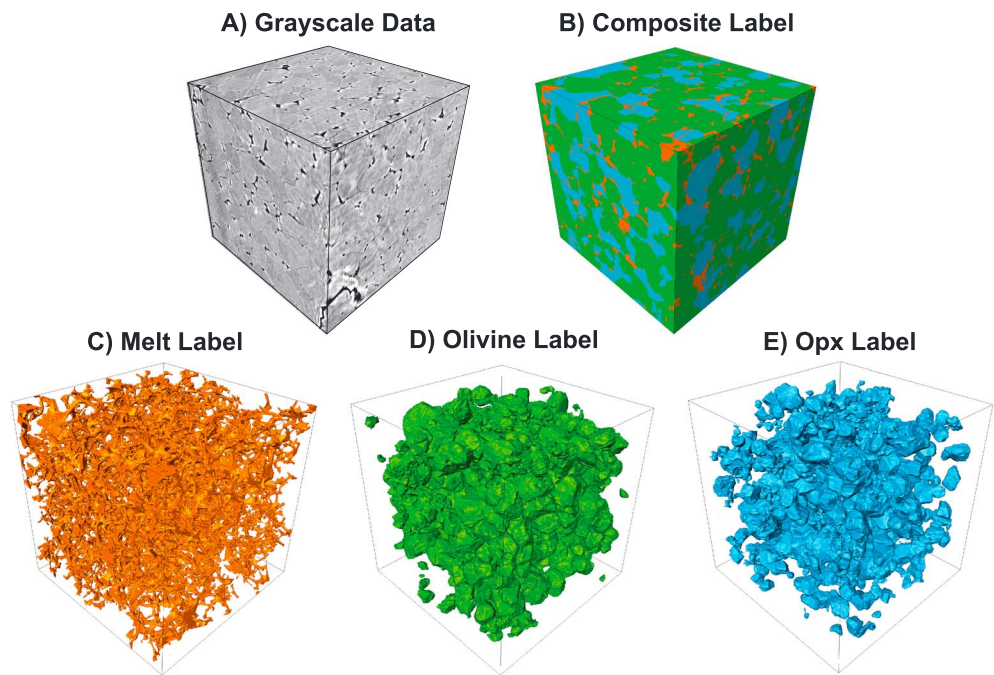
Figure 5. Illustrated workflow of data reduction technique. (a) Original gray scale subvolume. (b) Composite label image comprised, which is a superposition of the all the materials. (c–e) Label images of each material, which are cropped from Figure 5b to ease visualization of the materials. Border grains are removed from olivine and opx images prior to local melt fraction and grain size analysis.

novel, adaptive technique to quantify the melt fraction associated with each grain. First, an ellipsoid was fitted to each grain (Figure 7) using ellipsoid_fit copyright [*Petrov*, 2009], a script contributed to MatlabCentral (http://www.mathworks.com/matlabcentral). The principal lengths and orientations of the ellipsoid were eigenvalues and eigenvectors, respectively, of the ellipsoid fit parameters. Next, we uniformly dilated the fitted ellipsoid while keeping the same aspect ratio by multiplication of both major and minor axes by a growth parameter p. Local melt fractions were calculated by summing the number of melt voxels divided by the total number of voxels within each ellipsoidal envelope. The local melt fraction associated with each ellipsoidal envelope was thus obtained for every grain at various p values in the subvolume.
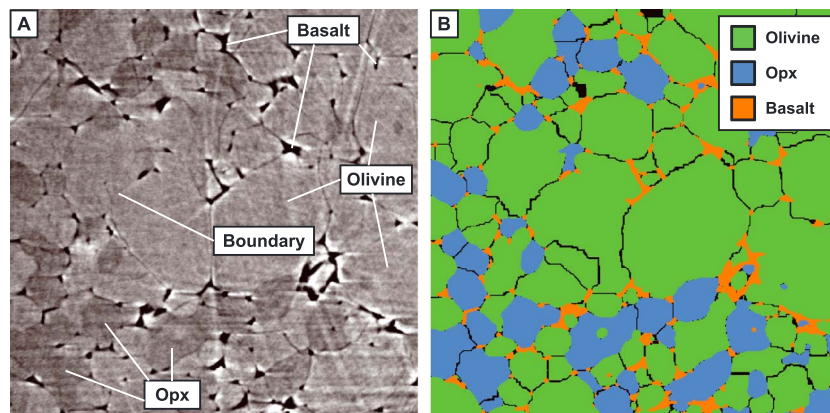
Figure 6. Demonstration of image segmentation by grain separation technique. (a) Gray scale image of 2-D slice through harzburgite-basaltic melt subvolume. Materials are identified with appropriate labels. (b) Label image after application of semiautomatic image segmentation by grain separation technique. The color is indicative of the material. Grain boundaries that were detected by the watershed transform are black. Comparing Figures 6a and 6b, it is clear that most grain boundaries are correctly identified. However, some are missed by the watershed transform, leading to grain clumps.
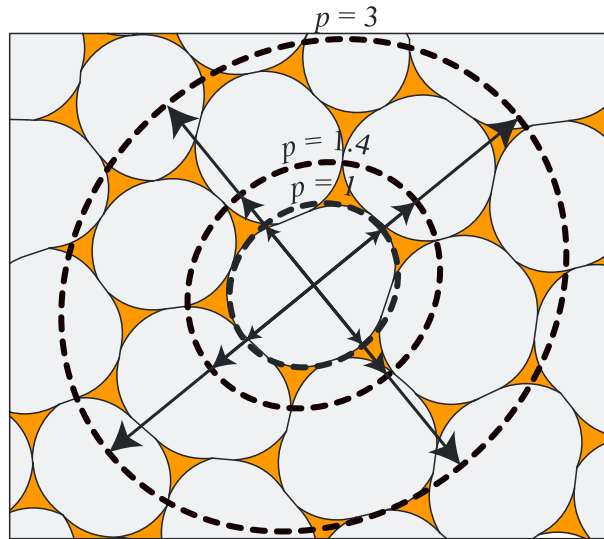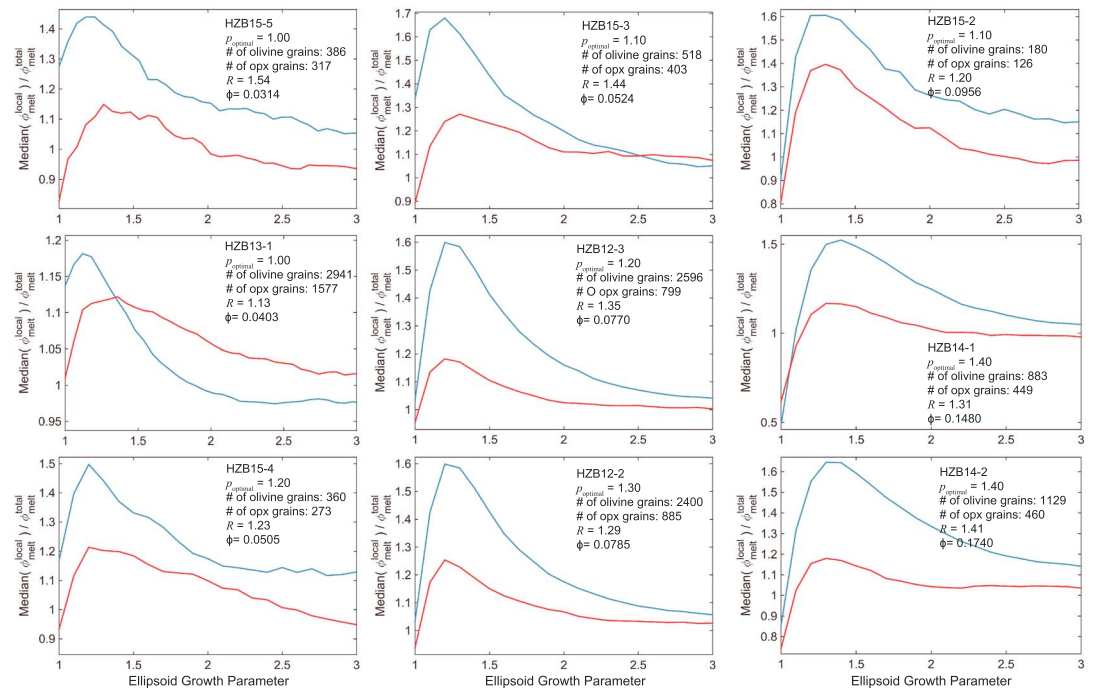
Figure 7. Schematic diagram of the local melt fraction analysis technique. Gray and orange represent grain and melt. Dotted lines are ellipsoid envelopes for different growth parameters $p = 1$, 1.4, and 3. The $p = 1$ ellipsoid is too small and misses melt. The $p = 3$ ellipsoid is too large and counts melt from other grains. $p = 1.4$ is approximately the optimal value that enclose the melt immediately surrounding the grain.

We discuss the characteristics of the local melt fraction distributions associated with olivine and opx grains. The median local melt fraction varies with the growth factor p. When the ellipsoids were too small, some melt regions associated with the grain were left out as the grain was not perfectly ellipsoidal and could jut out of the region of interest. Thus, the calculated values underestimated the local melt fraction at small p. Conversely, when the ellipsoids were too large, adjacent solid grains were included in the region of interest, again underestimating the local melt fraction (Figure 7). Thus, the best, albeit imperfect, estimate of local melt fraction was obtained for an intermediate value of p.

Lithologic melt partition is apparent by a systematic difference between the melt fraction around olivine grains and the melt fraction around opx grains. Evidently, this ratio depended on the chosen growth factor p. The value of p at which the maximum difference between the median local melt fraction of olivine and opx is observed is labeled $p_{optimal}$ in Figure 8. We observed that $p_{optimal}$ produced ellipsoidal envelopes that enclosed only melt adjacent to each grain and therefore generated the best available estimate of local melt fraction.

Figure 8. Median olivine (blue) and opx (red) local melt fractions of each subvolume plotted as a function of growth parameter p. The optimal value of p, at which the difference between olivine and opx median local melt fractions is the largest, is reported on each panel along with the number of grains taken into account and the melt partition ratio R at $p_{optimal}$.

Table 2. Summary of Harzburgite Results[a]

Subvolume	Dimensions (voxel^3)	ϕ_{melt}^{nom} (%)	ϕ_{melt} (%)	$\phi_{olivine}$ (%)	ϕ_{opx} (%)	$\phi_{olivine}/\phi_{opx}$ (%)	d (μm)	R
HZB13-1	$500 \times 500 \times 490$	2	4.03	67.3	28.7	2.35	18	1.13
HZB12-2	$500 \times 500 \times 500$	10	7.85	57.6	34.6	1.66	20	1.29
HZB12-3	$500 \times 500 \times 500$	10	7.70	61.2	31.1	1.97	20	1.35
HZB14-1	$500 \times 500 \times 500$	20	14.8	48.8	36.4	1.34	26	1.31
HZB14-2	$500 \times 500 \times 500$	20	17.4	44.8	37.8	1.19	22	1.41
HZB15-2	$450 \times 450 \times 400$	5	9.56	67.1	23.3	2.88	34	1.20
HZB15-3	$450 \times 450 \times 450$	5	5.24	66.8	28.0	2.39	23	1.44
HZB15-4	$450 \times 450 \times 300$	5	5.05	69.6	25.3	2.75	18	1.23
HZB15-5	$450 \times 450 \times 300$	5	3.14	78.8	18.1	4.36	17	1.54

[a]Numerical values in the first column represent the sample name and subvolume identification number. The second column has subvolume dimensions (measured in voxels) along the *x*, *y*, and *z* axis of the subvolume, respectively. The material volumetric proportions were calculated from the digital subvolumes. *d* is the geometric mean equivalent diameter. *R* is the melt partition ratio.

2.5. Characterizing Grain Size Distributions

Permeability depends on grain size. In order to isolate the change in permeability from a difference in grain size between subvolumes, we computed grain size distributions for each subvolume. The grain size distribution of each subvolume was determined by estimating the equivalent diameter of each grain. The equivalent diameter is defined as the diameter of a sphere having the same volume as the grain [*Miller et al.*, 2014, 2015].

The accuracy of the computed grain size distribution depends on the degree to which melt wets the surface of the grains. At this stage of the analysis, we enhanced the wetness of grain boundaries by applying an opening filter using "ball-shaped" kernel to the segmented grain label images. The "opened" images were not used in the calculation of local melt fractions or transport properties. A morphological watershed algorithm was used to approximate the location of the solid-solid boundaries. The equivalent diameter was then measured for each grain. The morphological watershed transform was completely automatic. Sometimes, the algorithm introduced artifacts. For example, when grain boundaries were mostly melt free, the morphological watershed transform counted multiple grains as a single grain (e.g., Figure 6), which led to larger uncertainties in grain size distribution for low melt fraction samples.

3. Results

3.1. Local Melt Fraction Distributions

Local melt fraction distributions were computed for each olivine or opx grain in each subvolume and reported against *p* in Figure 8. The largest ratio of median local melt fraction of olivine and opx in each subvolume was obtained for $p_{optimal}$ values ranging from 1.1 to 1.4.

The lithologic partitioning coefficient *R* is defined as

$$R = \phi_{ol}/\phi_{opx} \tag{3}$$

where ϕ_{ol} and ϕ_{opx} are the median local melt fractions at $p = p_{optimal}$ associated with olivine and opx grains, respectively. *R* is larger than 1 for all samples, indicating a consistently higher local melt fraction associated with olivine grains than with opx grains (Table 2). In different subvolumes, *R* varies between 1.1 and 1.6.

The local melt fraction and the total measured melt fraction of the subvolume generally converge at very large values of *p*, as the samples do not systematically exhibit large-scale segregation of olivine and opx (Figure 8). However, in some subvolumes, the local melt fraction does not subtend to the melt fraction measured over the subvolume. The existence of a measureable partitioning over length scales several times larger than the grain size may simply reflect the tendency of opx grains to clump together (Figure 6), but it could also be indicative of an as-yet unidentified long-range effect of lithologic melt partitioning.

3.2. Grain Size Distributions

Grain size distributions were conducted using the completely automated procedure described above. As a proxy for grain size, we computed the equivalent diameter distribution for olivine and opx in each subvolume (Figure 9).
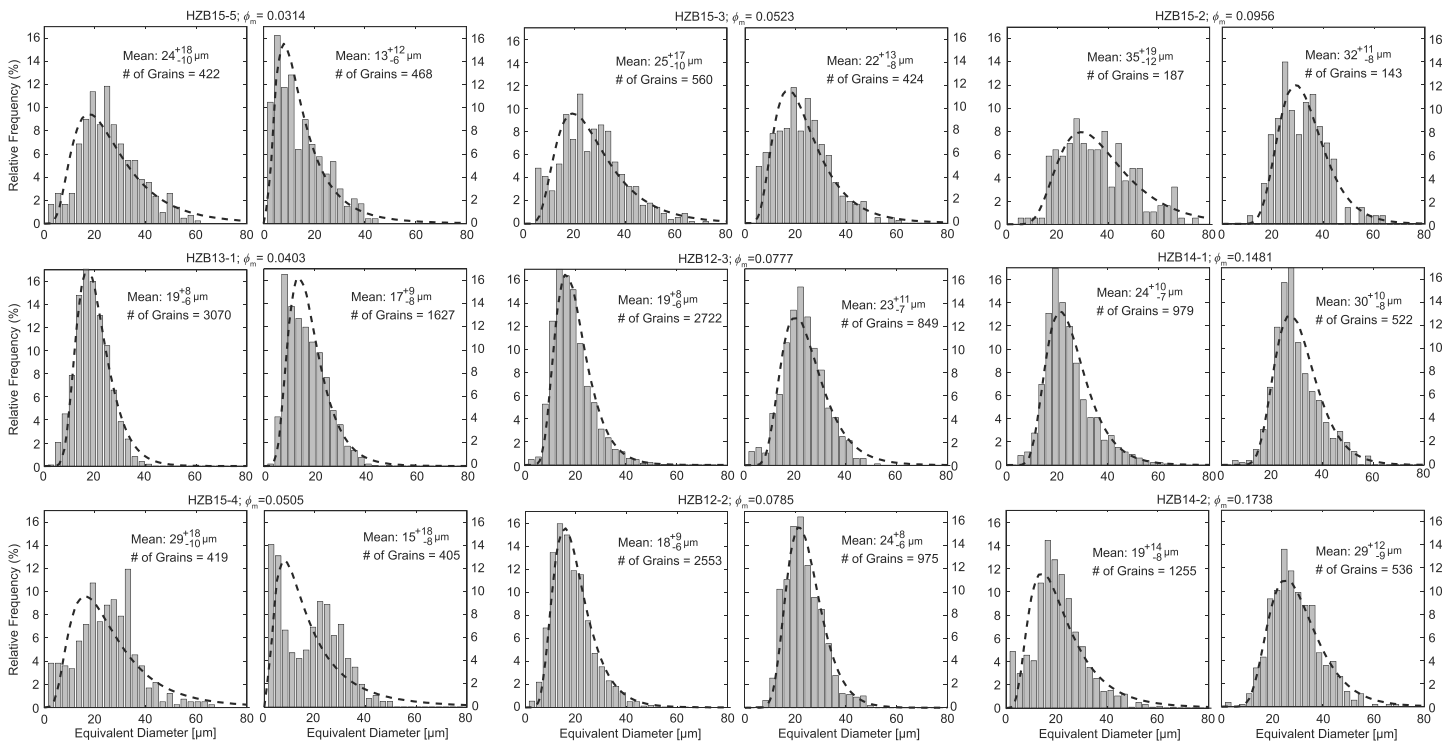
Figure 9. (left columns) Olivine and (right columns) opx equivalent diameter distributions measured for each subvolume. Mean and standard deviations are obtained by computing the geometric mean and (1σ) standard deviations. The number of grains used in statistics is also reported.

Equivalent diameter data appeared to follow lognormal distributions, which is expected for aggregates at textural equilibrium [*Wark and Watson*, 1998]. Correspondingly, we reported the geometric mean and standard deviation as the mean grain size and width of grain size distribution. As expected, subvolumes containing on the order of 1000 grains had narrower distributions. As noted in *Miller et al.* [2014], the automated watershed transform that was used to separate 3-D grain data produced a more accurate grain size distribution when the melt fraction is higher, since grain boundaries were more easily distinguished if they are wetted by melt. The frequency of melt-free triple junctions and dry grain-grain boundaries increased as the melt fraction decreases.
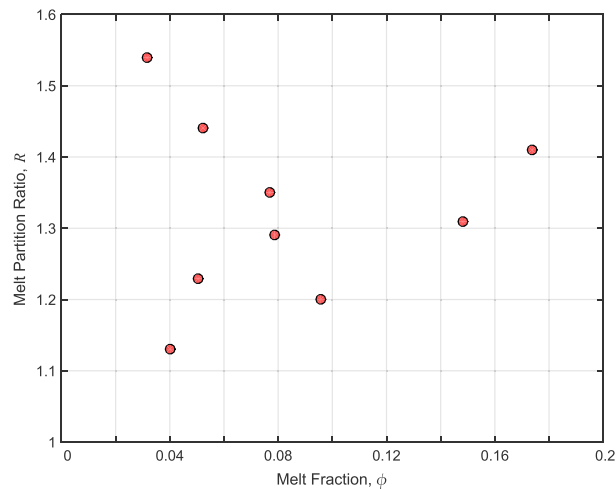
4. Discussion

4.1. Lithologic Melt Partitioning

In Figure 10, we report the lithologic partitioning coefficient R as a function of the melt content. R is always greater than 1, ranging from 1.1 to 1.6 for the melt fractions tested. R does not seem to vary systematically with total melt content ϕ_{total}, although it should be noted that the uncertainty associated with R could not be rigorously constrained with the available data, since to our knowledge, there is currently no method for estimating error bars on volumetric proportions measured from image analysis. Refer to *Miller et al.* [2014, 2015] for an estimate on absolute bounds for melt fraction.

The absence of a systematic relation between R and total melt content is probably due to the relatively small difference in apparent dihedral angle near olivine and opx grains. A similar phenomenon is observed when studying the interfacial energy of two mineral/melt aggregates in contact, although the predicted R in that case is larger than seen here [*Park and Yoon*, 1985; *Cheadle*, 1989; *Lupulescu and Watson*, 1999]. R is expected to depend most on total melt content when ϕ_{total} is large and the difference in dihedral angle between the two aggregates is large. For the intimate mixture of mineral types that is present in our samples, melt in tubules along grain edges is rarely in contact with only olivine or only pyroxene. When melt tubules are lined with different mineral type, the apparent dihedral angle that controls melt topology is intermediate between the dihedral angles of the pure mineral phases [*Zhu and Hirth*, 2003]. Thus, although pure olivine and pure

Figure 10. Melt partitioning coefficient plotted as a function of melt fraction.

orthopyroxene have drastically different dihedral angles, the contrast in effective dihedral angle around olivine and opx grains is reduced compared to that of the pure phases. Nevertheless, the difference in thermodynamic environment is sufficient for olivine grains to be surrounded on average by 10 to 60 vol % more melt than opx grains ($R = 1.1$ to 1.6).

The melt partitioning observed in our experimental charges is less than the factor of 2 to 5 expected from the dihedral angles of pure olivine-melt and opx-melt aggregates [*Park and Yoon*, 1985; *Watson*, 1999]. That is likely due to the absence of these pure end-member configurations in our experimental charges: melt is present in a thermodynamic environment that always includes olivine and opx, albeit in different proportions. The dihedral angle of a three-component mixture (olivine-opx-melt) is expected to be intermediate between the two end-members [*Zhu and Hirth*, 2003], although a specific value is impossible to predict due to the importance of the unknown olivine-opx interfacial energy. Moreover, the dihedral angle is expected to vary based on the local proportion of opx [*Zhu and Hirth*, 2003], which invalidates statistical methods of measuring dihedral angles using two-dimensional sections [e.g., *Holness*, 2005]. Although a detailed study of the relation between dihedral angle and local opx abundance is beyond of scope of this paper, it can safely be stated that the variations of dihedral angle are less than expected from end-member mineralogies, explaining why R is 1.6 or less in our samples.

4.2. Influence of Lithologic Melt Partitioning on Permeability

The permeability of partially molten mantle rock is a function of the melt network geometry and thus the wetting properties of the constituent mineral components. Despite the predominance of polycrystalline rocks in nature, current estimates of mantle rock permeability only consider a single mineralogy. Fortunately, the digital format of our melt geometry data presented an opportunity to use numerical fluid flow simulations to estimate the permeability of our synthetic harzburgitic rocks.

We used Avizo® XLab Hydro to solve Stokes' equations for the pressure and velocity fields within the space occupied by each melt volume. Darcy's law was applied to the simulation results to estimate the permeability of each harzburgite subvolume. The grain size dependence of permeability was accounted for by normalizing each permeability estimate by the geometric mean grain equivalent diameter. Results are compared with the permeabilities of pure olivine and basaltic melt subvolumes from *Miller et al.* [2014] in Figure 11a.

Harzburgite permeability does not deviate significantly from the olivine permeability-melt fraction power law. Lithologic melt partitioning can affect the permeability of the aggregate in two fundamental ways. First, focusing melt into olivine-rich regions increases the hydraulic radius of melt channels adjacent to olivine grains while reducing it next to opx grains—this effect is quantitatively discussed in section 4.4. The effect of changing hydraulic radius on permeability, however, is slight since olivine and opx grains have nominally homogeneous mixing. Second, lithologic melt partitioning can affect the connectivity of the melt geometry. Triple junctions adjacent to opx grains need a threshold melt fraction of ~0.03 to sustain connectivity [*von Bargen and Waff*, 1986]. For a local melt fraction less than 0.03, opx-rich regions begin to lose connectivity with the melt network. Due to the tendency for percolation pathways to form in porous media [*Martys and Garboczi*, 1992; *David*, 1993; *Miller et al.*, 2015], loss of network connections of ~40% is needed to change permeability significantly [*Zhu and Hirth*, 2003].

In order to obtain a notion of melt interconnectivity at $\phi < 0.03$, we examined an opx-rich subvolume from our harzburgite samples containing a melt fraction of only 0.014. The melt geometry is visualized in Figure 11b.
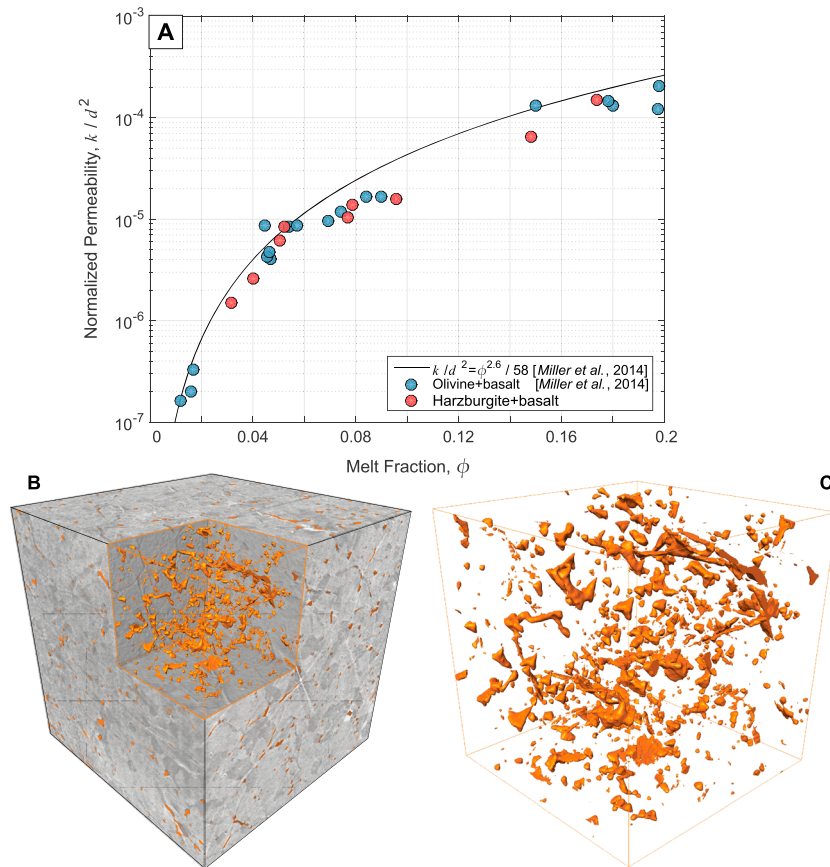
Figure 11. Permeability analysis of harzburgite subvolumes. (a) Permeability of harzburgite + melt and olivine + melt samples plotted against subvolume melt content. Each permeability value was normalized by the geometric mean equivalent diameters of the associated subvolume. Results for olivine + basalt subvolumes and the power law relation (solid line) are from *Miller et al.* [2014]. (b) Visualization of a subvolume that contains a melt fraction of ~0.01. (c) Visualization of the melt isosurface extracted from the low melt fraction subvolume in Figure 11b to show that most of the melt in contained within isolated bodies.

It should be noted that melt content and permeability of this sample cannot be reliably determined because the melt channels are so thin that they approach the resolution of our instrumentation (700 nm per voxel). For example, we cannot confidently report whether or not melt is present along a perceived dry grain boundary. Nevertheless, volume renderings of the μCT data and corresponding label image (Figure 11c) show that melt almost exclusively resides in isolated pockets at grain corners, as expected for low melt fractions surrounded by opx. As a result, the permeability of the subvolume is zero.

Network models that take lithologic partitioning into account show that low melt fractions (i.e., $\phi < 0.02$) cannot percolate through the rock if it contains at least 60% opx [*Zhu and Hirth*, 2003]. This is consistent with opx-rich regions losing connectivity at $\phi \sim 0.03$ due to lithologic partitioning. Although we prefer not to report the permeability of this sample in Figure 11a due to uncertainties, it is clear that the inclusion of pyroxene reduces melt interconnectivity and therefore the permeability of the samples with the lowest melt fraction.

4.3. Electrical Conductivity

The presence of a connected melt network causes partially molten rocks to be at least an order of magnitude more electrically conductive than unmelted mantle rock. Using the magnetotelluric method, it is possible to invert for the subsurface electrical conductivity. Accurate interpretations of melt content from electrical conductivity profiles of the upper mantle require a well-constrained constitutive relation between bulk electrical conductivity and melt fraction, which we provide here with numerical direct current simulations. Simulations
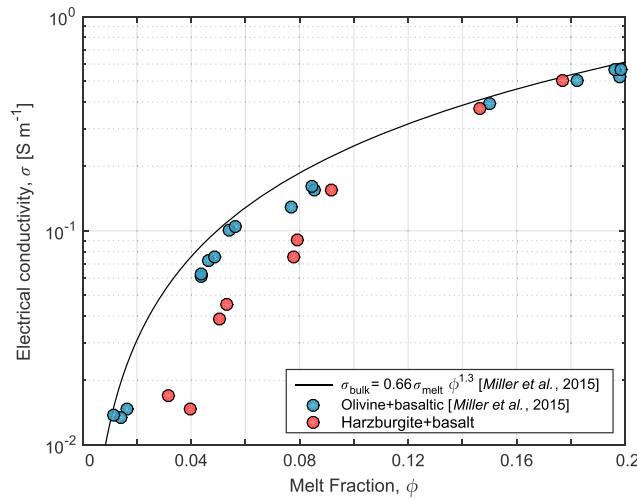
Figure 12. Electrical conductivity of harzburgite + melt and olivine + melt samples determined by direct current simulation. Results for olivine + basalt subvolumes are from *Miller et al.* [2015].

were conducted on the melt-solid composite geometries using our in-house MATLAB-based software FDECC [*Miller et al.*, 2015], which solves Laplace's equation, assuming electrical conductivities of $7.53\,S\,m^{-1}$ for basaltic melt [*ten Grotenhuis et al.*, 2005] and $0.009\,S\,m^{-1}$ for olivine [*Constable*, 2006] at 1475°C. The conductivity of opx was assumed to be the same as olivine. The results are plotted in Figure 12. To summarize, electrical conductivity of opx-bearing subvolumes was less than electrical conductivity of opx-free subvolumes when $\phi_{total} < 0.10$. Electric flux depends on the radius of melt pathways to the second power, whereas fluid is proportional to that radius to the fourth power. Therefore, fluid flow tends to form preferential percolation pathways—i.e., pathways that contain >90% of mass flux but electricity conducts more diffusively through the melt network [*David*, 1993; *Miller et al.*, 2015]. As a result, electricity is able to flow through the thinner melt tubules that are associated with opx. Since more current is traveling through less efficient conductors, the overall effect is a decrease in the bulk conductivity.

4.4. Transport Properties Deduced From End-Member Mixing Models

The harzburgitic samples examined in this study are composed of an intimate mixture of olivine and opx grains with an interstitial melt network. We previously determined the permeability and electrical conductivity of olivine/melt aggregates [*Miller et al.*, 2014, 2015], and in this study, we show that the addition of opx does not change permeability but reduces electrical conductivity when melt fraction is low. In this section, we discuss mixing models that provide estimates of transport properties of olivine/opx/melt mixtures based on the properties of end-member olivine/melt and opx/melt aggregates. These models are general enough to be applicable to other mineral assemblages where lithologic melt partitioning would be expected.

Permeability and conductivity are typically expressed as a power law of melt fraction; although what follows is using symbol σ for conductivity, the formalism is exactly equivalent for permeability. For a mixture of olivine only and melt with porosity ϕ, we typically write

$$\sigma_o = s_o \left(\frac{\phi}{f_o} \right)^{n_o} \tag{4}$$

where s_o and f_o are scaling numbers that depend on mineralogy and grain size. From our previous work on olivine $n_o = 2.5$ for permeability [*Miller et al.*, 2014] and 1.5 for conductivity [*Miller et al.*, 2015]. We expect a similar relation to hold for opx/melt aggregates:

$$\sigma_p = s_p \left(\frac{\phi}{f_p} \right)^{n_p} \tag{5}$$

At $\phi > 3\%$, we expect the power law exponent n_p for opx/melt aggregates to be very close to n_o. However, as discussed in section 4.2, the permeability exponent n_p would be much higher at $\phi < 3\%$ because the larger dihedral angle between opx and melt causes loss of connectivity [*von Bargen and Waff*, 1986; *Zhu and Hirth*, 2003]. The conductivity exponent n_p for pure opx/melt aggregates is not known at this point. However, we expect the conductivity exponent n_p of opx/melt aggregates to be higher than the conductivity exponent of olivine/melt aggregates, n_o, since conductivity is more sensitive to thin conduits.

For convenience, the relations for bulk conductivity are expressed using ϕ_E, the porosity for which the conductivity of the olivine/melt and opx/melt aggregates are similar, and σ_E that conductivity

$$\phi_E = (s_p/s_o)^{\frac{1}{n_o-n_p}}, \sigma_E = s_o \phi_E^{n_o} = s_p \phi_E^{n_p} \tag{6}$$

so that

$$\sigma_o = \sigma_E (\phi/\phi_E)^{n_o}, \sigma_p = \sigma_E (\phi/\phi_E)^{n_p} \tag{7}$$

Let us consider now an aggregate composed of olivine, opx, and melt. The solid is composed of a fraction F_p of opx and $F_o = 1 - F_p$ of olivine. If the porosities near olivine and opx are ϕ_o and $\phi_p = \phi_o/R$, where R is the lithologic partitioning coefficient, the porosity of the sample as a whole is

$$\phi_{total} = F_o \phi_o + F_p \phi_p = \phi_o + F_p(\phi_p - \phi_o) = \phi_o \left[1 - F_p(1 - 1/R)\right] \tag{8}$$

or equivalently, $\phi_o = P\phi_{total}$, with

$$P = \left[1 - F_p(1 - 1/R)\right]^{-1} \tag{9}$$

The conductivity of the aggregate can be estimated from the end-member mineralogies assuming a particular configuration or mixing model. Five kinds of averages are most commonly encountered in the literature.

The arithmetic average is most appropriate for a situation where the various phases (olivine and opx) are aligned in the transport direction. The harmonic average represents a structure where the phases form layers perpendicular to the transport direction. The geometric average represents a case where the phases are intimately mixed and is most successful to represent natural microstructures [*Madden*, 1976]. *Hashin and Shtrikman* [1962] proposed averaging laws for mixtures based on variational theorems. When restricted to a two-phase aggregate, their relations result in two bounds, each understood as a variation for the transport property for a pure phase. These bounds are often referred to as an upper and lower bound, as it is assumed one phase is weaker than the other. However, the relation between σ in the olivine and pyroxene regions changes at ϕ_E. Therefore, we refer to these bounds as the olivine Hashin-Shtrikman and pyroxene Hashin-Shtrikman bounds.

For clarity, the various averages and bounds are most easily expressed using σ_o the value of σ in the olivine-melt regions, taking partitioning into account, and ρ, the ratio of σ in the opx and olivine regions.

$$\sigma_o = \sigma_E \left(\frac{P\phi_{total}}{\phi_E}\right)^{n_o} \tag{10}$$

$$\rho = \frac{\sigma_p}{\sigma_o} = \left(\frac{P\phi_{total}}{\phi_E}\right)^{n_p-n_o} R^{-n_p} \tag{11}$$

arithmetic average : $\quad \sigma = F_o\sigma_o + F_p\sigma_p \Leftrightarrow \sigma = \sigma_o \left\lfloor 1 - F_p(1-\rho)\right\rfloor \tag{12}$

harmonic average : $\quad \sigma^{-1} = F_o\sigma_o^{-1} + F_p\sigma_p^{-1} \Leftrightarrow \sigma = \sigma_o \left[1 - F_p\left(1 - \rho^{-1}\right)\right]^{-1} \tag{13}$

geometric average : $\sigma = \sigma_o^{F_o}\sigma_p^{F_p} \Leftrightarrow \sigma = \sigma_o \rho^{F_p} \tag{14}$

pyroxene ("lower") Hashin-Shtrikman bound :
$$\sigma = \sigma_p + \frac{F_o}{(\sigma_o - \sigma_p)^{-1} + F_p(3\sigma_p)^{-1}}$$
$$\Leftrightarrow \sigma = \sigma_o \rho \left[1 + \frac{1-F_p}{F_p}\left(\frac{1}{3} + \frac{1}{F_p}\frac{\rho}{1-\rho}\right)^{-1}\right] \tag{15}$$

olivine ("upper") Hashin-Shtrikman bound :
$$\sigma = \sigma_o + \frac{F_p}{(\sigma_p - \sigma_o)^{-1} + F_o(3\sigma_o)^{-1}}$$
$$\Leftrightarrow \sigma = \sigma_o \left[1 + \frac{F_p}{1-F_p}\left(\frac{1}{3} + \frac{1}{1-F_p}\frac{1}{\rho-1}\right)^{-1}\right] \tag{16}$$

The five mixing relations are illustrated in Figure 13 for $n_p > n_o$ with two cases: either no lithological partitioning ($R = 1$) or the partitioning observed in our samples ($R = 1.5$). The porosity for which more transport occurs in pyroxene/melt regions increases, as partitioning increases the melt fraction in the olivine region, for equal total porosity. The crossover porosity is given by

$$\phi_C = \phi_T P^{-1} R^{\frac{n_p}{n_p-n_o}} \tag{17}$$
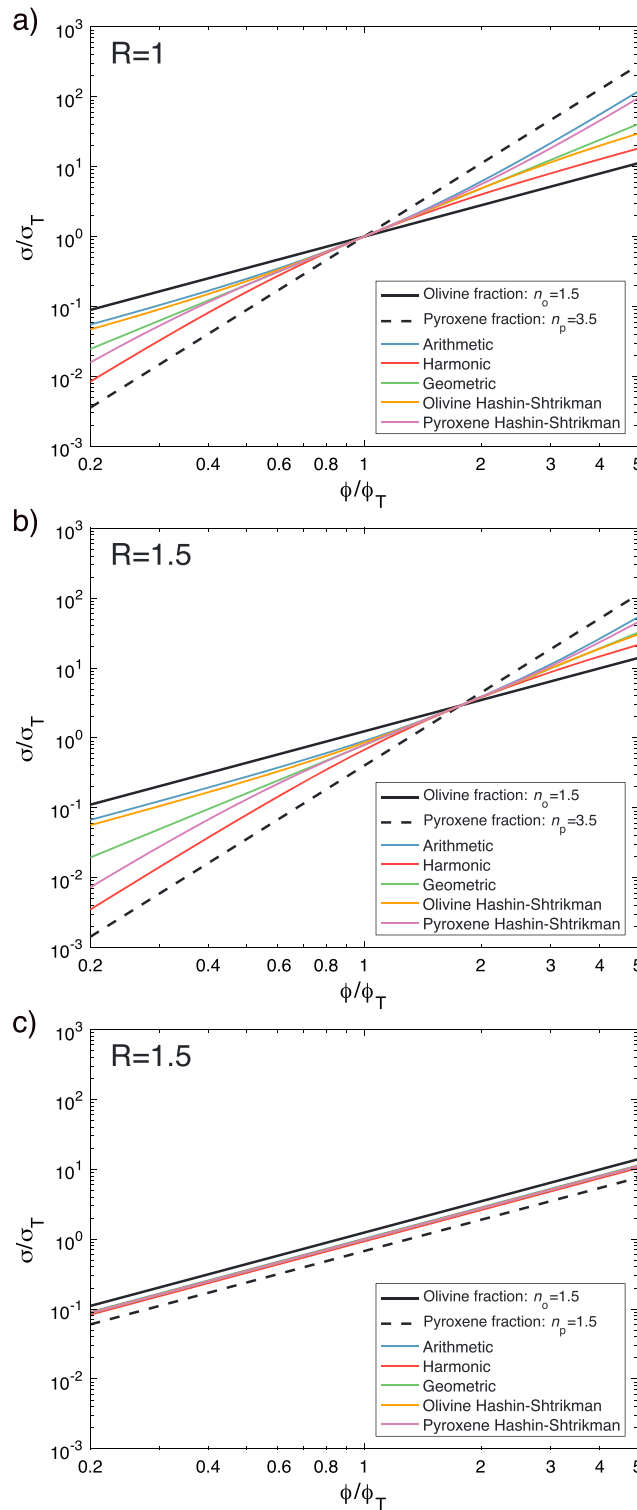
Figure 13. Analytical models for transport through harzburgite ($F_P = 0.4$) aggregate based on end-member olivine and pyroxene transport properties (equations (12)–(16)) with (a) $R = 1$, $n_o = 1.5$, and $n_p = 3.5$; (b) $R = 1.5$, $n_o = 1.5$, and $n_p = 3.5$; and (c) $R = 1.5$ and $n_o = n_p = 1.5$.

Significant deviations from a power law (straight lines in Figure 13) are observed only very close to that crossover point. The net effect of partitioning is to slightly reduce σ.

If we assume the olivine/melt or an opx/melt mixtures have the same power law exponent, i.e., $n_p = n_o$, all the mixing relations become power laws (Figure 13c). Although transport in the olivine regions is larger than in the pyroxene regions due to partitioning, transport in the mixture is very close from that in a pure phase + melt aggregate. This explains the remarkable correspondence between the permeability of the harzburgite/melt and olivine/melt samples in Figure 11. A stronger effect of opx on permeability is expected if more opx is present in the sample or if the melt fraction is so small that interconnection is no longer possible in opx-rich regions. Until the percolation threshold is reached, fluid flow proceeds along olivine-dominated region and the permeability of the sample is hardly affected by the presence of pyroxene.

The conductivity simulations show that the harzburgite/melt samples have lower conductivity than the olivine/melt samples when the melt fraction is smaller than ~0.12. A similar behavior is observed with the geometric mixing model or pyroxene Hashin-Shtrikman bound (Figure 13) if $\phi_E \sim 0.12$. It may be expected that the conduction of the harzburgitic samples would exceed that of the olivine samples if the melt fraction exceeded that of our most porous sample, $\phi > 0.17$.

4.5. Implications for Melt Focusing Mechanisms in Upper Mantle

In the partially molten regions of upper mantle, melt focusing may be controlled by the interplay between lithologic partitioning, pyroxene dissolution, and mechanical shear. In particular, we propose that lithologic partitioning should enhance the effects of the reaction infiltration

instability (RII). The RII is a positive feedback processes in which dissolution of opx in a harzburgitic mantle by a melt that is undersaturated with respect to opx leads to an increase in melt flux that further promotes opx dissolution [*Daines and Kohlstedt*, 1994; *Kelemen et al.*, 1995, 1997]. Numerical modeling using multiphase flow theory has shown that the RII is capable of forming high melt fraction dunite conduits whose thicknesses range from tens to thousands of meters [*Aharonov et al.*, 1995; *Kelemen et al.*, 1995; *Spiegelman et al.*, 2001]. More recently, the RII has been confirmed to produce high melt fraction dunite conduits in laboratory experiments [*Pec et al.*, 2015]. If these dunite conduits are present in the upper mantle, they provide a mineralogical heterogeneity that could segregate melt by way of lithologic melt partitioning.

Lithologic melt partitioning may further the formation of high melt fraction conduits that result from RII. *Spiegelman et al.* [2001] suggests that once the opx supply has been depleted, the melt fraction will continue to eat away at the side of the conduits while the reaction stops in dunite channels. As melt rises continuously by buoyancy, the dunite conduit is abandoned as the RII and the active channel migrate laterally to locations where opx is actively dissolving. However, field observations of banded dunite-harzburgite formations in the Oman ophiolite [*Kelemen et al.*, 1995] suggest that dunite conduits are persistent localized features of the upper mantle. Therefore, an additional mechanism is required to sustain high melt fraction in the dunite conduits.

Lithologic melt partitioning may provide such a mechanism. Assuming that sufficient time is available for lithologic partitioning to move melt over distances larger than grain scale, it might help to drive melt into the dunite channels, replenishing the melt supply in the high melt fraction dunites. As the opx fraction in the dissolution channels decreases, we are approaching situations where the dihedral angle of the pure mineral phase becomes important and therefore R increases. Once the melt starts dissolving opx and producing olivine-rich regions, more Si-undersaturated melt is drawn into olivine-rich regions, which further enhances opx dissolution. This process continues until opx is exhausted, and localized melt flux can persist in olivine-rich dunite channels. Thus, the RII and lithologic partitioning feed back into one another.

4.6. Implications for Mantle Xenoliths

Mineralogical effects on the permeability of mantle rocks may have important implications for interpreting trace element partitioning in peridotite xenoliths. In particular, lithium (Li), which has a diffusivity in mantle rocks that is two to three orders of magnitude larger than that of other trace elements [*Richter et al.*, 2003], has the potential to be a sensitive indicator of melt-rock interactions in the upper mantle. Previous studies [e.g., *Frey and Green*, 1974; *Rudnick and Ionov*, 2007] have reported strong Li disequilibria—both elemental and isotopic—between peridotite xenoliths and the "normal" mantle, which is consistent with an event of mantle metasomatism, i.e., grain boundary infiltration of a Li-rich melt or fluid [*Rudnick and Ionov*, 2007]. Despite preferential enrichment of Li in clinopyroxene (cpx) over olivine compared to equilibrium partitioning, refractory harzburgite xenoliths exhibit higher overall enrichment of Li compared to fertile lherzolite xenoliths [*Rudnick and Ionov*, 2007].

One interpretation of this result invokes the wetting properties of peridotite mineral components. If the permeability of olivine-rich peridotite (harzburgite) is higher than that of olivine-poor peridotite (lherzolite), harzburgite xenoliths will likely experience higher flux of Li-rich melt than lherzolite xenoliths. Thus, lithologic partitioning will favor incorporation of Li through grain boundaries in the most refractory xenoliths. Whether Li enrichment will actually take place likely depends on the degree to which equilibration is possible and may be limited by kinetic and other disequilibrium processes.

5. Conclusions

We used high-resolution X-ray microtomography to image the 3-D microstructure of partially molten harzburgites that contain nominal melt fraction between 0.02 and 0.20. A novel methodology was applied to resolve the density contrast at olivine-basalt, opx-basalt, and olivine-opx interfaces. We computed local melt fraction distributions for olivine and opx grains by fitting ellipsoidal envelopes to each grain. We found that melt partitions in about a 1.1 to 1.5 ratio between olivine and opx for total nominal melt fractions 0.02 to 0.20, which we attribute to spatial variations in surface energy associated with low surface energy density olivine interfaces and high surface energy density opx interfaces. Though we did not observe a change in permeability from pure olivine to opx-bearing partially molten aggregates containing greater than melt fraction of 0.03, a qualitative analysis of one subvolume containing melt fraction of 0.014 suggests that permeability does

drop with respect to an all olivine-basaltic melt sample containing the same melt fraction. Depending on the orientation of olivine and opx-rich regions in the mantle, lithologic melt partitioning may enhance melt transport in the mantle. Also, by showing that permeability did not change with 40 vol % opx, we conclusively rule out permeability change for all lower volume proportions of opx. Electrical conductivity, on the other hand, was lowered by the presence of 40 vol % opx.

References

Aharonov, E., J. A. Whitehead, P. B. Kelemen, and M. Spiegelman (1995), Channeling instability of upwelling melt in the mantle, *J. Geophys. Res.*, *100*(B10), 20,433–20,450, doi:10.1029/95JB01307.

Allwright, J., and R. F. Katz (2014), Pipe Poiseuille flow of viscously anisotropic, partially molten rock, *Geophys. J. Int.*, *199*(3), 1608–1624, doi:10.1093/gji/ggu345.

Bulau, J. R., H. S. Waff, and J. A. Tyburczy (1979), Mechanical and thermodynamic constraints on fluid distribution in partial melts, *J. Geophys. Res.*, *84*(B11), 6102–6108, doi:10.1029/JB084iB11p06102.

Chapman, D., W. Thomlinson, R. Johnston, D. Washburn, E. Pisano, N. Gmür, Z. Zhong, R. Menk, F. Arfelli, and D. Sayers (1997), Diffraction enhanced X-ray imaging, *Phys. Med. Biol.*, *42*(11), 2015–2025.

Cheadle, M. J. (1989), Properties of texturally equilibrated two-phase aggregates, PhD thesis, Cambridge Univ., 156 pp.

Condomines, M., P. Morand, and C. J. Allégre (1981), ^{230}Th-^{238}U radioactive disequilibria in tholeiites from the FAMOUS zone (Mid-Atlantic Ridge, 36° 50′N): Th and Sr isotopic geochemistry, *Earth Planet. Sci. Lett.*, *55*, 247–256.

Constable, S. (2006), SEO3: A new model of olivine electrical conductivity, *Geophys. J. Int.*, *166*(1), 435–437, doi:10.1111/j.1365-246X.2006.03041.x.

Cooper, R. F., and D. L. Kohlstedt (1982), Interfacial energies in the olivine-basalt system, *Adv. Earth Planet. Sci.*, *12*, 217–228.

Cooper, R. F., and D. L. Kohlstedt (1984), Solution-precipitation enhanced diffusional creep of partially molten olivine-basalt aggregates during hot-pressing, *Tectonophysics*, *107*(3), 207–233.

Daines, M. J., and D. L. Kohlstedt (1994), The transition from porous to channelized flow due to melt/rock reaction during melt migration, *Geophys. Res. Lett.*, *21*(2), 145–148, doi:10.1029/93GL03052.

David, C. (1993), Geometry of flow paths for fluid transport in rocks, *J. Geophys. Res.*, *98*(B7), 12,267–12,278, doi:10.1029/93JB00522.

Dick, H. (1989), Abyssal peridotites, very slow spreading ridges and ocean ridge magmatism, *Geol. Soc. London Spec. Publ.*, *42*(1), 71–105.

Dowd, B. A., G. H. Campbell, D. P. Siddons, R. B. Marr, V. V. Nagarkar, S. V. Tipnis, and L. Axe (1999), Developments in synchrotron x-ray computed microtomography at the National Synchrotron Light Source, *Proc. SPIE*, *1*, 224–236.

Fitzgerald, R. (2000), Phase-sensitive X-ray imaging, *Phys. Today*, *53*(7), 23–26, doi:10.1063/1.1292471.

Frey, F. A., and D. H. Green (1974), The mineralogy, geochemistry and origin of lherzolite inclusions in Victorian basanites, *Geochim. Cosmochim. Acta*, *38*(7), 1023–1059, doi:10.1016/0016-7037(74)90003-9.

Gürsoy, D., F. De Carlo, X. Xiao, and C. Jacobsen (2014), TomoPy: A framework for the analysis of synchrotron tomographic data, *Synchrotron Radiat.*, *21*(5), 1188–1193.

Hashin, Z., and S. Shtrikman (1962), A variational approach to the theory of the effective magnetic permeability of multiphase materials, *J. Appl. Phys.*, *33*(10), 3125–3131.

Holness, M. B. (2005), Melt-solid dihedral angles of common minerals in natural rocks, *J. Petrol.*, *47*(4), 791–800, doi:10.1093/petrology/egi094.

Holtzman, B. K., and D. L. Kohlstedt (2007), Stress-driven melt segregation and strain partitioning in partially molten rocks: Effects of stress and strain, *J. Petrol.*, *48*(12), 2379–2406, doi:10.1093/petrology/egm065.

Holtzman, B. K., D. L. Kohlstedt, M. E. Zimmerman, F. Heidelbach, T. Hiraga, and J. Hustoft (2003), Melt segregation and strain partitioning: Implications for seismic anisotropy and mantle flow, *Science*, *301*(5631), 1227–1230, doi:10.1126/science.1087132.

Iwamori, H. (1994), ^{238}U-^{230}Th-^{226}Ra and ^{235}U-^{231}Pa disequilibria produced by mantle melting with porous and channel flows, *Earth Planet. Sci. Lett.*, *125*, 1–16.

Johannes, W., P. Bell, H. Mao, A. Boettcher, D. Chopman, J. Hays, R. Newton, and F. Seifert (1971), An interlaboratory comparison of piston-cylinder pressure calibration using the albite-breakdown reaction, *Contrib. Mineral. Petrol.*, *32*(1), 24–38.

Johns, R. A., J. S. Steude, L. M. Castanier, and P. V. Roberts (1993), Nondestructive measurements of fracture aperture in crystalline rock cores using X ray computed tomography, *J. Geophys. Res.*, *98*(B2), 1889–1900, doi:10.1029/92JB02298.

Jull, M., P. B. Kelemen, and K. Sims (2002), Consequences of diffuse and channelized porous melt migration on U-series disequilibria, *Geochim. Cosmochim. Acta*, *66*(23), 4133–4148.

Kelemen, P. B., N. Shimizu, and V. J. M. Salters (1995), Extraction of mid-ocean-ridge basalt from the upwelling mantle by focused flow of melt in dunite channels, *Nature*, *375*(6534), 747–753, doi:10.1038/375747a0.

Kelemen, P. B., G. Hirth, N. Shimizu, M. Spiegelman, and H. J. Dick (1997), A review of melt migration processes in the adiabatically upwelling mantle beneath oceanic spreading ridges, *Philos. Trans. R. Soc. London Ser., A*, *355*(1723), 283–318.

Lupulescu, A., and E. B. Watson (1999), Low melt fraction connectivity of granitic and tonalitic melts in a mafic crustal rock at 800°C and 1 GPa, *Contrib. Mineral. Petrol.*, *134*(2-3), 202–216, doi:10.1007/s004100050479.

Madden, T. (1976), Random networks and mixing laws, *Geophysics*, *41*(6), 1104–1125.

Martys, N., and E. J. Garboczi (1992), Length scales relating the fluid permeability and electrical conductivity in random two-dimensional model porous media, *Phys. Rev. B*, *46*(10), 6080–6090.

Miller, K. J., W. Zhu, L. G. J. Montési, and G. A. Gaetani (2014), Experimental quantification of permeability of partially molten mantle rock, *Earth Planet. Sci. Lett.*, *388*, 273–282, doi:10.1016/j.epsl.2013.12.003.

Miller, K. J., L. G. J. Montési, and W. Zhu (2015), Estimates of olivine–basaltic melt electrical conductivity using a digital rock physics approach, *Earth Planet. Sci. Lett.*, *432*, 322–341, doi:10.1016/j.epsl.2015.10.0034.

Münch, B., P. Trtik, F. Marone, and M. Stampanoni (2009), Stripe and ring artifact removal with combined wavelet-Fourier filtering, *EMPA Act.*, *17*(10), 34–35, doi:10.1364/OE.17.008567.

Newman, S., R. C. Finkel, and J. D. MacDougall (1983), ^{230}Th-^{238}U disequilibrium systematics in ocean tholeiites from 21°N on the East Pacific Rise, *Earth Planet. Sci. Lett.*, *65*, 17–33.

Paganin, D., S. C. Mayo, T. E. Gureyev, P. R. Miller, and S. W. Wilkins (2002), Simultaneous phase and amplitude extraction from a single defocused image of a homogeneous object, *J. Microsc.*, *206*(1), 33–40, doi:10.1046/j.1365-2818.2002.01010.x.

Park, H., and D. N. Yoon (1985), Effect of dihedral angle on the morphology of grains in a matrix phase, *Metallurg. Trans. A*, *16*(5), 923–927, doi:10.1007/BF02814844.

Pec, M., B. K. Holtzman, M. Zimmerman, and D. L. Kohlstedt (2015), Reaction infiltration instabilities in experiments on partially molten mantle rocks, *Geology*, *43*(7), 575–578, doi:10.1130/G36611.1.

Petrov, Y. (2009), Ellipsoid fit. [Available at https://www.mathworks.com/matlabcentral/fileexchange/24693-ellipsoid-fit*MATLAB Central File Exchange*. Retrieved April 1, 2013.]

Qi, C., D. L. Kohlstedt, R. F. Katz, and Y. Takei (2015), Experimental test of the viscous anisotropy hypothesis for partially molten rocks, *Proc. Natl. Acad. Sci. U.S.A.*, *112*(41), 12,616–12,620, doi:10.1073/pnas.1513790112.

Richter, F. M., A. M. Davis, D. J. DePaolo, and E. B. Watson (2003), Isotope fractionation by chemical diffusion between molten basalt and rhyolite, *Geochim. Cosmochim. Acta*, *67*(20), 3905–3923, doi:10.1016/S0016-7037(03)00174-1.

Rudnick, R. L., and D. A. Ionov (2007), Lithium elemental and isotopic disequilibrium in minerals from peridotite xenoliths from far-east Russia: Product of recent melt/fluid-rock reaction, *Earth Planet. Sci. Lett.*, *256*(1-2), 278–293, doi:10.1016/j.epsl.2007.01.035.

Smith, C. (1964), Some elementary principles of polycrystalline microstructure, *Metall. Rev.*, *9*(33), 1–48.

Smith, C. S. (1948), Grains, phases, and interfaces: An interpretation of microstructure, *Trans. Am. Inst. Min. Metall. Eng.*, *175*(1), 15–51, doi:10.1007/s11661-010-0215-5.

Spiegelman, M., P. B. Kelemen, and E. Aharonov (2001), Causes and consequences of flow organization during melt transport: The reaction infiltration instability in compactible media, *J. Geophys. Res.*, *106*(B2), 2061–2077, doi:10.1029/2000JB900240.

ten Grotenhuis, S. M., M. R. Drury, C. J. Spiers, and C. J. Peach (2005), Melt distribution in olivine rocks based on electrical conductivity measurements, *J. Geophys. Res.*, *110*, B12201, doi:10.1029/2004JB003462.

Toramaru, A., and N. Fujii (1986), Connectivity of melt phase in a partially molten peridotite, *J. Geophys. Res.*, *91*(B9), 9239–9252, doi:10.1029/JB091iB09p09239.

Volpe, A., and P. Hammond (1991), 238U-230Th-226Ra disequilibria in young Mount St. Helens rocks: Time constraint for magma formation and crystallization, *Earth Planet. Sci. Lett.*, *107*(3), 475–486, doi:10.1016/0012-821X(91)90094-X.

von Bargen, N., and H. S. Waff (1986), Permeabilities, interfacial areas and curvatures of partially molten systems: Results of numerical computations of equilibrium microstructures, *J. Geophys. Res.*, *91*(B9), 9261–9276, doi:10.1029/JB091iB09p09261.

Waff, H. S., and J. R. Bulau (1979), Equilibrium fluid distribution in an ultramafic partial melt under hydrostatic stress conditions, *J. Geophys. Res.*, *84*(B11), 6109–6114, doi:10.1029/JB084iB11p06109.

Wark, D. A., and E. B. Watson (1998), Grain-scale permeabilities of texturally equilibrate, monomineralic rocks, *Earth Planet. Sci. Lett.*, *164*(3), 591–605, doi:10.1016/S0012-821X(98)00252-0.

Watson, E. B. (1999), Lithologic partitioning of fluids and melts, *Am. Mineral.*, *84*, 1693–1710.

Watson, H. C., and J. J. Roberts (2011), Connectivity of core forming melts: Experimental constraints from electrical conductivity and X-ray tomography, *Phys. Earth Planet. Inter.*, *186*(3), 172–182, doi:10.1016/j.pepi.2011.03.009.

Zhu, W., and G. Hirth (2003), A network model for permeability in partially molten rocks, *Earth Planet. Sci. Lett.*, *212*(3), 407–416, doi:10.1016/S0012-821X(03)00264-4.

Zhu, W., G. A. Gaetani, F. Fusseis, L. G. J. Montési, and F. De Carlo (2011), Microtomography of partially molten rocks: Three-dimensional melt distribution in mantle peridotite, *Science*, *332*(6025), 88–91, doi:10.1126/science.1202221.